DOI: 10.21062/mft.2025.036 http://www.journalmt.com

Titanium Alloy Turning Machining Model and Quality Analysis Based on Finite Element Analysis

Zhenhua Wang (0009-0006-6191-0907)*, Haifang Yin (0009-0000-4557-548X)
Engineering Training Center, Shandong Huayu University of Technology, Dezhou, 253000, China. E-mail*: 15053489783@163.com

Workpiece manufacturing of titanium alloy is widely used in various high-end fields. In this study, finite element analysis of titanium alloy turning process is carried out, and the turning process is modeled by using material properties and intrinsic equations. Then, the power transmission of centerless lathe is controlled in the machining process, so as to obtain the performance calculation of different process parameters on cutting force, chips and residual stress. The simulation and experimental data analysis results showed that the cutting depth and cutting speed had a significant effect on the cutting force and residual stress. The optimized parameters could significantly improve the surface quality of machining. The study combined finite element modeling with mechanical property analysis to solve the problem of insufficient characterization of thermal softening effects in traditional analysis, and significantly improved the surface quality and accuracy of titanium alloy machining. This study fills the gap in modeling the mechanical behavior of precision machining on centerless lathes and has important technical guidance value for the efficient manufacturing of key aerospace components. It also provides a new technological avenue for optimizing the performance of titanium alloy materials in future machining and parts manufacturing.

Keywords: Finite element analysis, Titanium alloy material, Finishing process, Cutting force, Residual stresses

1 Introduction

Since titanium alloys (TAs) are lightweight, strong, corrosion resistant, and can withstand high temperatures, they are widely used in a variety of cutting-edge industries, including consumer electronics, chemical equipment, aerospace, and medical devices [1-2]. Specifically, mechanical engineering and materials processing are crucial to industrial applications [3]. The excellent properties of TAs make them a serious challenge for process technology, but modern technologies have significantly improved their processing performance. Three-dimensional printing and metal injection molding technologies are the main directions for TA processing [4-5]. Finite element technology is crucial to the intricate processing of TAs, including cutting, extrusion, and thermoforming, since computer performance advances quickly. By mimicking the processing techniques, it lowers labor costs and material costs, optimizes processing parameters, and enhances processing quality [6].

In recent years, scholars at home and abroad have studied TA turning processing technology in great detail. With regard to the problem of TA turning process, Ahmad A et al. proposed to use orthogonal array and analysis of variance etc. to design and evaluate the process parameters experimentally, which in turn proved the high accuracy of the model [7]. Regarding the TA turning process, Yang H et al. suggested using an electroplastic-assisted method to lower the material's tensile strength and springback. The feasibility of electro-plastic assisted cutting and turning could be demonstrated by the comparison of cutting force (CF) [8]. Wang D et al. analyzed the fatigue properties of TAs and proposed a mathematical model using bending fatigue tests and turning machining. This study analyzed the effect of parameters and concluded that proper machining techniques will prolong the life of the material [9]. Palanivel R et al. proposed the use of polycrystalline diamond tool inserts for cutting TAs with respect to their turning performance and concluded that their machining performance was improved by comparison of surface smoothness and tool wear [10]. Thus, in the machining and manufacturing of TAs of different nature, the existing studies have developed better processing techniques for their machining process, which have improved the quality of performance to some extent.

Finite element analysis (FEA) methods have also been widely studied in turning machining process. Li L et al. suggested using a finite element model (FEM) to simulate the electrical discharge machining process, which increased the machining process's prediction accuracy [11]. Yu H et al. proposed to use the FEM method to describe the micromachining process of their materials in order to improve the cutting performance (CP) of graphene-reinforced aluminum-metal matrix composites. They then confirmed the accuracy

of the model experimentally to increase the amplitude and fluctuation of the CF [12]. Grossi, Niccolò et al. proposed the use of finite element method to calculate the tool paths for compensating the diameter error for the turning of slender parts. This study demonstrated that compensated tool paths in the turning of slender workpieces could reduce the diameter error through the estimation of FEM and CF model [13]. To assess the thermal behavior and material removal rate for the powder hybrid electric discharge machining process, Surani K et al. suggested using FEA. In contrast to the traditional method, this study's two-dimensional axisymmetric transient thermal model increased the material heat flux by enabling the determination of material removal at various currents [14]. The FEA method is feasible and effective in predicting and calculating the relevant properties during processing in different directions.

In summary, the utilization of TA turning and FEA is relatively mature at present, which improves the relevant performance and prolongs the service life in each type of machining process. However, when machining, there is a lot of friction between the tool and the workpiece since TA has poor heat conductivity. Thus, it leads to the phenomenon of condensation of TA workpiece materials during machining, and it is difficult to dissipate heat. Based on this, the study uses the FEA method and the intrinsic equation and material properties to establish the machining model of centerless lathe finish turning TA. The innovation lies in the use of FEA and its simulation model to extract the mechanical properties during the turning and cutting process. To determine the ideal settings to raise the workpiece's quality and machining efficiency, comparisons are also done between the test bench and simulation modeling.

2 Methods and materials

The study utilizes the FEA method for simulation modeling of the TA turning process, and then uses the intrinsic equations and material property calculations to derive the mechanical properties of the TA material. Finally, an FEM of the TA material cutting process is developed to simulate the cutting process and predict the mechanical behavior of the material process parameters.

2.1 FEA method for turning process

Due to the difficult-to-machine properties of TA materials, it is difficult to meet the surface quality requirements of TAs by ordinary turning machining process, so the study builds a centerless lathe to finish machining the surface of TA workpieces to remove the surface defects or oxidized layer. To ensure the machining quality, the study utilizes advanced simulation for engineering and sciences (ABAQUS) to simulate the machining process of TA workpieces, and analyzes the lathe machining quality in depth by simulating the cutting indexes. The steps of ABAQUS software for workpiece processing are shown in Fig. 1.

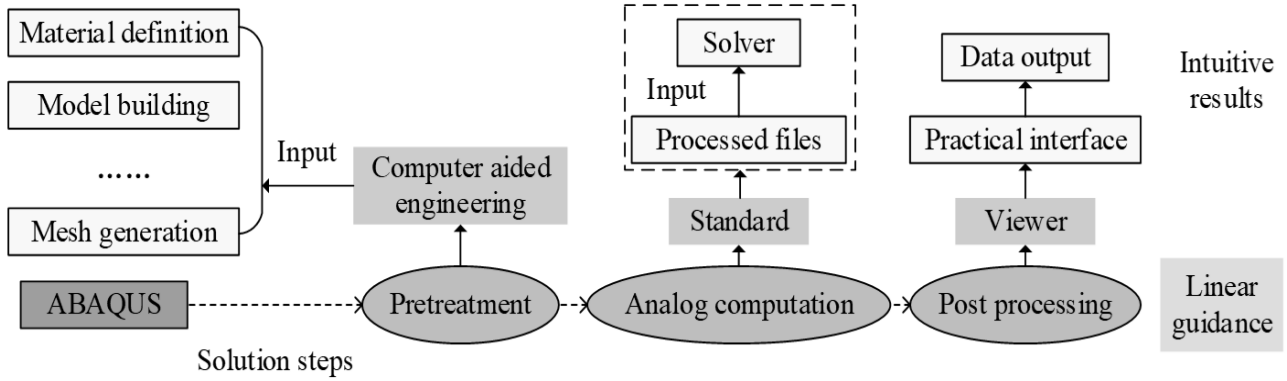

Fig. 1 *Basic solving steps of BAQUS software*

In Fig. 1, the solution steps of ABAQUS software are pre-processing of computer-aided engineering, numerical simulation calculation, and post-processing at the user's end. Among them, the pre-processing in the artificial interactive interface to enter the definition of the material, load, boundary conditions, to provide a data base for simulation calculations and modeling environment. The simulation calculation analyzes the processed files in the solver, and its calculation efficiency and accuracy are related to the pre-processing. Finally, the data is output in the interface to visualize the calculation results and provide dynamic information results on the performance of the workpiece.

The key to the FEA method is numerical simulation, which first discretizes the structure of the workpiece material. Each unit of the discretized structure has a corresponding node, which can be converted into an ensemble by combining these nodes. In FEA, the geometric data and physical properties of each unit are calculated in order to establish the unit matrix [15-16]. Equation (1) displays the computation.

$$K^a = \frac{F^a}{\varphi^a} \quad (1)$$

Where:
K …The stiffness matrix;
F^a …The force vector of the unit node;
a …The unit serial number;
φ^a The node displacement.

After discretization, the finite element equations are shown in Equation (2).

$$F = K \times \varphi \quad (2)$$

Where:
F …The load vector of the overall structure;
φ …The overall node displacement vector.

Under the overall finite element square, the properties of the actual material are utilized to calculate the finite element equations for each node.

After the processing of ABAQUS software, the three-dimensional FEM of the finishing turning machining process is constructed. Meanwhile, to refine the mesh area of surface cutting, the study focuses on the treatment of high temperature environment of TA while simplifying its cutting process. In the FEA, the mesh division of the finishing turning process is shown in Fig. 2.

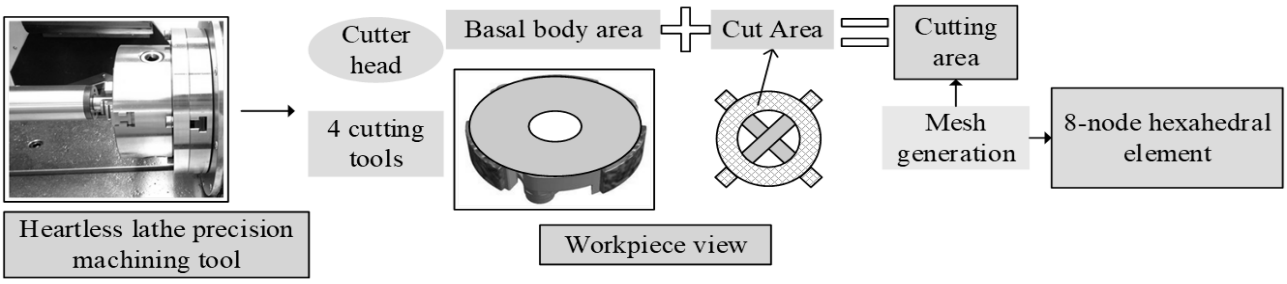

Fig. 2 *Schematic diagram of finite element mesh division for turning machining*

Fig. 2 illustrates the importance of FEA in the finishing turning process and how its mesh partitioning can more accurately model the shape and process of chip formation. The use of different mesh density stress subdivision techniques for the tool, workpiece and chip in the vicinity of the contact surface between the two can reduce the number of meshes and the distortion they cause, in addition to increasing simulation accuracy. The structure of finishing machining tool is a cutter plate and 4 tools and the center of the cutter plate is selected around the spindle. Moreover, the mesh type used for the workpiece is 8-node hexahedral cell, which can improve the computational accuracy in the finite cloud simulation with large deformation and high strain rate.

2.2 Calculation of finite element constitutive equations and material properties

According to the turning process and FEA method, the cutting process of finish machining tool is better mesh refinement. To streamline the calculation time, the cutting process will ignore the tool wear and follow the rigid-plasticity method of FEA, which considers the tool as a rigid body. During the turning process, a significant amount of heat is generated by the friction between the tool and the chip. The tool-chip contact surface can be separated into distinct areas due to varying levels of heat dissipation. The expression is shown in Equation (3).

$$\begin{cases} f_H = \mu & f_H < \sigma \\ f_J = \sigma & f_J > \mu \end{cases} \quad (3)$$

Where:
f_H …The sliding friction stress;
μ …The coefficient of friction;
f_J …The bonding friction stress;
σ …The ultimate shear flow stress of the material.

During the titanium turning process, its metal forming problem acquires properties such as internal stresses depending on the displacement route of the material [17]. The elastic-plastic deformation is shown in Equation (4).

$$d\varepsilon = d\varepsilon_E + d\varepsilon_S \quad (4)$$

Where:
$d\varepsilon$ …The strain inkrement;
E, S …The elastic and plastic states, respectively.

Equation (5) depicts the elastic state.

$$\tau = D_e \varepsilon \quad (5)$$

Where:
τ …The equivalent stress;
D_e …The elastic matrix;
e …The elastic modulus;
ε …The strain.

Yielding of the material occurs when the maximum shear stress of the workpiece satisfies the threshold value, as shown in Equation (6).

$$\varsigma_{\max} = m \quad (6)$$

Where:
$\varsigma_{\max}$ …The maximum shear stress;
m …The shear stress at which the material yields.

The stress expression is shown in Equation (7).

$$P_f = \left[\left(\lambda_1 - \lambda_2\right)^2 - 4m^2\right] \times \left[\left(\lambda_2 - \lambda_3\right)^2 - 4m^2\right] \times \left[\left(\lambda_3 - \lambda_1\right)^2 - 4m^2\right] = 0 \quad (7)$$

Where:

P_f …The principal stress;

λ_1, λ_2, λ_3 …Three-way stresses.

Next, yielding occurs when the stress at a point within the material reaches the deformation criterion. The destructive force generated when a material is subjected to shear is shown in Equation (8).

$$\varsigma_L = N - \theta_L \times \tan\alpha \quad (8)$$

Where:

ς_L, θ_L …The tangential and positive stresses on the fracture surface of the material, respectively;

N …The cohesive force;

α …The angle of internal friction.

Yielding under static water pressure is shown in Equation (9).

$$P_Z = \phi \times I_1 + \sqrt{J_2} - \nu = 0 \quad (9)$$

Where:

P_Z …The yield stress (YS) of the material under static hydraulic pressure;

I_1 …The first invariant of the stress tensor;

J_2 …The second invariant of the bias stress;

ϕ, ν …The material properties, respectively.

Combining the above equations, the stress balance of the rigid-plastic finite element equation is shown in Equation (10).

$$\tau_{i,j,i} = 0 \quad (10)$$

Where:

$\tau_{i,j,i}$ …The force in different directions.

The present constitutive equation is shown in Equation (11).

$$\begin{cases} \dot{\eta}_{i,j,i} = \dot{\gamma} \times \dot{\tau}_{i,j,i} & \bar{\tau} = \sqrt{\frac{3}{2}\left(\dot{\tau}_{i,j} \times \dot{\tau}_{i,j}\right)^{\frac{1}{2}}} \\ \dot{\gamma} = \frac{3}{2} \times \frac{\bar{\eta}}{\bar{\tau}} & \bar{\eta} = \sqrt{\frac{3}{2}\left(\dot{\eta}_{i,j} \times \dot{\eta}_{i,j}\right)^{\frac{1}{2}}} \end{cases} \quad (11)$$

Where:

$\bar{\tau}$ …The equivalent stress of the constitutive equation;

$\dot{\eta}$, $\dot{\tau}$ …States under stress;

$\dot{\gamma}$ …The state of the overall structure under stress;

$\bar{\eta}$ …The equivalent strain rate.

The parameters of TA turning process are used in the constitutive equation as shown in Equation (12).

$$\tau = \left(X + Y\psi^n\right) \times \left(1 + C\ln\frac{\dot{\psi}}{\dot{\psi}_0}\right) \times \left[1 - \left(\frac{T - T_W}{T_R - T_W}\right)^R\right] \quad (12)$$

Where:

τ …The overall degree of multiple stresses in the interior of the material;

X, Y …The YS at the lowest strain rate and the degree of hardening in plastic deformation, respectively;

T …The dynamic temperature;

T_W …The coefficient of linear expansion at room temperature;

T_R …The temperature at which the material is converted from a solid to a liquid.

In plastic deformation of TA material, ψ represents its axial strain and n is the power index between true stress and true strain. However, under high strain rate conditions, C is the strength of change in YS. $\dot{\psi}$ is the degree of plastic deformation accumulated in the TA material during loading, while $\dot{\psi}_0$ is the rate at which the material undergoes deformation per unit time. The equivalent strain rate of the TA material is shown in Equation (13).

$$\dot{\psi}_f = \left[G_1 + G_2 \exp\left(G_3 \times \frac{z}{b}\right)\right] \times \left[1 + G_4 \ln\left(\frac{\dot{\psi}}{\dot{\psi}_0}\right)\right] \times \left(1 + G_5\right) \quad (13)$$

Where:

$\dot{\psi}_f$ …The equivalent strain rate of the materiál;

G …The damage constant;

z, b …Static pressure and material deformation pressure, respectively.

An efficient theory for the surface quality of the finishing turning process is the fact that the material separates from the chip more quickly when the workpiece breaks during the turning process. When the material's equivalent strain rate reaches the limit value, the damage starts to change continuously, which ultimately results in the chip.

2.3 Surface residual stress and quality effects of turning operations

According to the FEA theory and the calculation of TA material properties, the simulation model of the finishing turning machining process can simulate the

mechanical behavior between the tool and the workpiece, so as to predict the change of the CF academic parameters and the generation of chips. The power transfer of centerless lathe is shown in Fig. 3.

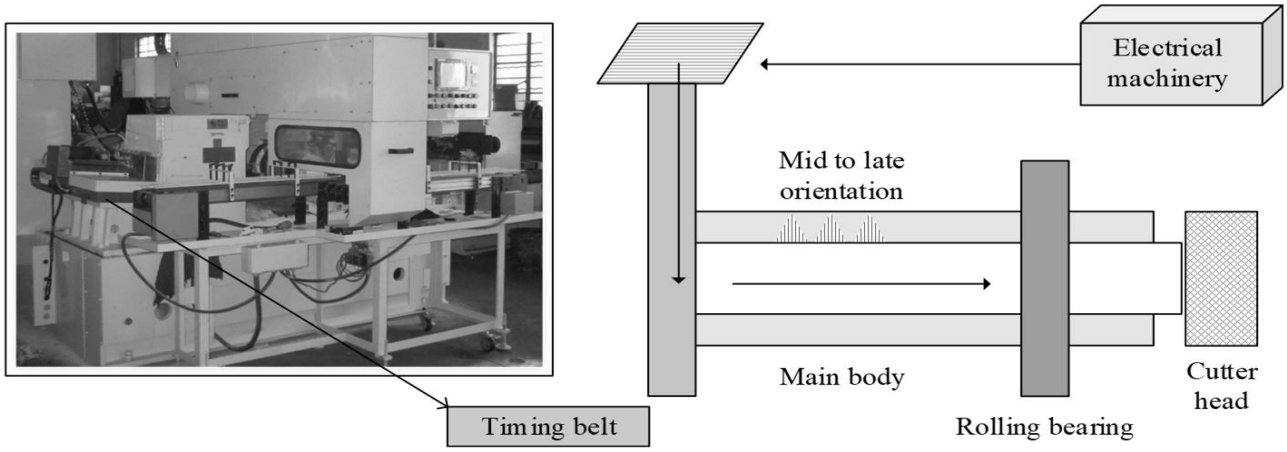

Fig. 3 *Power transmission diagram of centerless lathe*

Fig. 3 shows the cutting test and chip surface removal for finishing turning operations. The operation is carried out on a centerless lathe whose spindle current and speed are driven and controlled by a motor. After that sensors are set up for the timing belt and guiding equipment to collect the acceleration signals. Afterward, the cutter plate and its four tools are rotated at high speed under the power transfer from the rolling spindle to perform the surface cutting work on the workpiece material [18-19]. Based on the sequence of power transmission, the total efficiency of centerless lathe is calculated as shown in Equation (14).

$$O = O_1 \times O_2 \times O_3^2 \times O_4^3 \times O_\xi \tag{14}$$

Where:

O …The total efficiency of the overall transmission;

O_1, O_2 …The transmission efficiency of coupling and synchronous belt respectively;

O_3 …The transmission efficiency of rolling bearing;

O_4 …The transmission efficiency of the guide;

O_ξ …The transmission efficiency of the main CF.

In the cutting process will produce a certain amount of energy loss, as well as the torque of TA cutting. Therefore, the main CF of TA in lathe cutting process is shown in Equation (15).

$$\begin{cases} P_J = P_d \times O \\ P_J = \dfrac{T_J \times n}{9550} \\ T_J = 4 \times T \end{cases} \tag{15}$$

Where:

P_J …The tool operating power;

P_d …The running power of the motor;

T_J, n …The torque and rotational speed of the tool cutting process, respectively;

T …The torque and $T = f_Q \times \dfrac{G}{2}$ (f_Q is the main CF and G is the damage constant).

In addition, during the finishing turning process, the friction between the workpiece and the tool can affect the surface quality and residual stress (RS), as shown in Fig. 4.

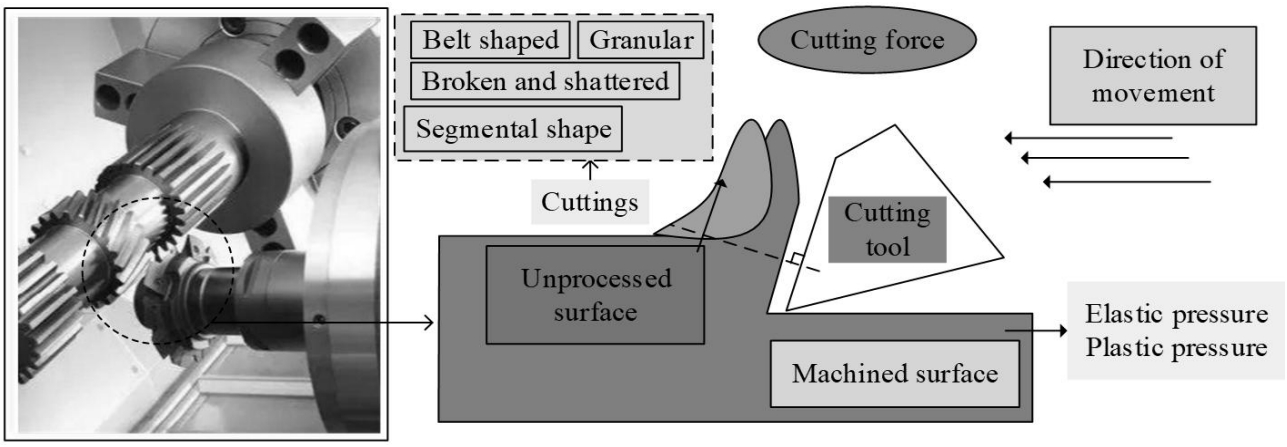

Fig. 4 *Schematic diagram of cutting process and chip formation process*

Fig. 4 demonstrates the action between the tool and the workpiece throughout the turning process as well as the contact between the surface of the workpiece and the tip of the tool. Under power operation, the workpiece material is friction and cutting under the action of the tool tip, which makes the appearance of chips on the surface layer, and thus completes the machined surface. The tip of the tool ends its elastic-plastic deformation state after finishing the surface machining. Throughout the cutting process, various stresses are generated between the tip and the workpiece. When the mechanical behavior ends, the stresses that remain inside the workpiece maintain its properties such as stability and strength.

According to the turning process and stress relationship, the surface RS can judge the CP and its quality. To enhance the surface quality of the TA turning process, the impact of feed rate and depth of cut (DOC) on RS during the turning process is also examined.

3 Results

Based on the FEA and the calculation of the principal equations, the TA turning machining model established by the study can analyze the main CF and RS. Moreover, the finite element simulation model and the test bench are utilized to compare the turning process and stress performance, which in turn verifies the reliability of the research method.

3.1 Simulation results of turning process and CF

According to the FEA and mechanical characteristic calculation of TA turning process, the study simulates the turning process of centerless lathe for testing. Under the setup of centerless lathe turning process experiment table, its tool selection is YT15 tungsten-titanium-cobalt carbide tool. INV3018CT high-precision data acquisition instrument and data acquisition and signal processing system software are used to collect and analyze the spindle current, rotational speed and signals during the experiment.

In the TA turning model, the relative distance traveled by the cutting tool for every one-week rotation is the tool travel. Different tool travel, DOC, spindle speed (SS) on the workpiece contact area is different, resulting in different CF. The results are shown in Fig. 5.

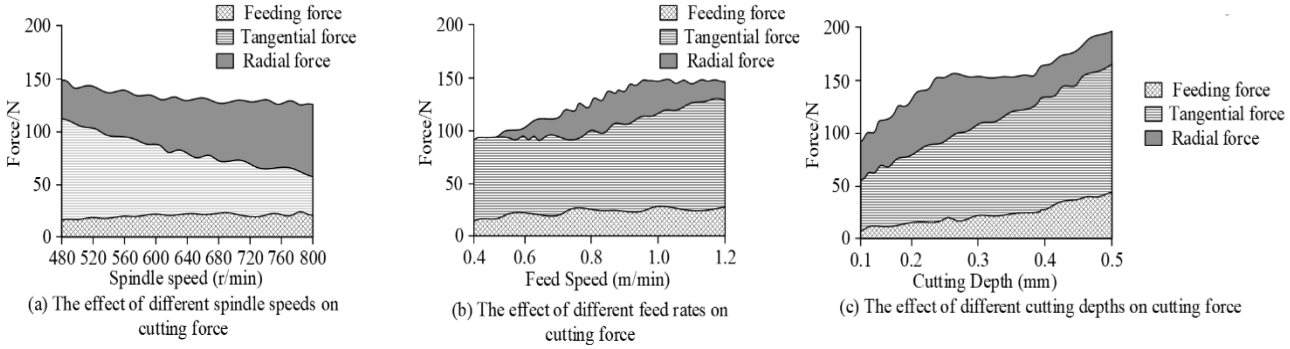

(a) The effect of different spindle speeds on cutting force

(b) The effect of different feed rates on cutting force

(c) The effect of different cutting depths on cutting force

Fig. 5 *The effect of different process parameters on CF*

In Fig. 5(a), the variation of CF is clearly inconsistent with the increase of SS, where the variation of feed force is the smallest, which is basically below 30N. However, the tangential and radial forces are significantly lower. At a rotational speed of 480 r/min, the maximum pair of stresses is 110N and 150N, respectively. The CF rises as the tool travel speed increases, as seen in Fig. 5(b). With increases of up to 135N and 150N, respectively, the tangential and radial forces exhibit the most notable increase among them. The depth of incision has the greatest effect on CF, as shown in Fig. 5(c). The tangential force in this instance grows most noticeably up to 150N. Whereas, the radial force does not change significantly between 0.25mm and 0.35mm, after which it rises rapidly up to 200N. Following the experimental CF results of the centerless lathe, the study contrasts the experimental and predicted CF values. The results are shown in Fig. 6.

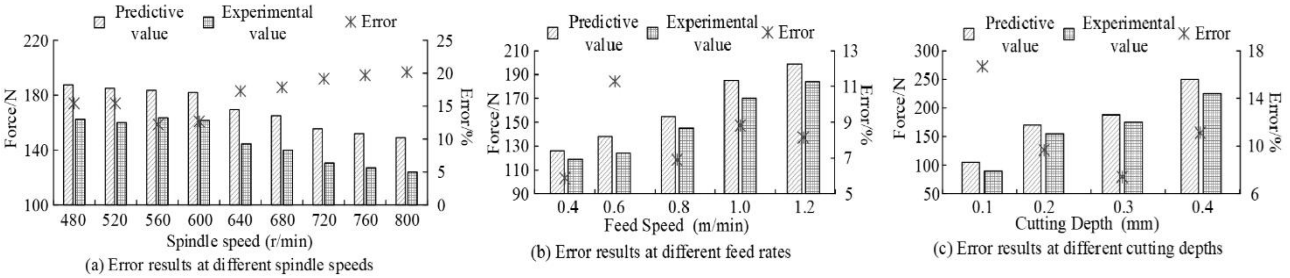

(a) Error results at different spindle speeds

(b) Error results at different feed rates

(c) Error results at different cutting depths

Fig. 6 *Comparison of CF simulation results and experiments under different process parameters*

According to Fig. 6(a), there is essentially a 25N discrepancy between the simulation and experimental results of the CF under the SS. When the speed is 800r/min, the experimental CF is 149N, while the simulation results in 124N. Fig. 6(b) displays that when the tool travel speed is 0.8m/min, the experimental moment result of CF is 185N, while the simulated moment result is 170N. Fig. 6(c) illustrates that the variation of CF is minimized when the DOC is 0.2mm and 0.3mm. In this case, the outcomes are 170N and 188N, while the corresponding simulation results are 155N and 175N, with an overall difference in torque between 13N and 25N.

To further illustrate the reliability and accuracy of the simulation modeling, the study compares the simulation and experiment on the generated chips. Table 1 displays the findings.

Tab. 1 *Simulation and experimental results of chip morphology*

Determine value	**Feed speed 1.0m/min, chip depth 0.3mm**		
Spindle speed	480r/min	640r/min	800r/min
Simulation	Strip shaped chips, longer and less prone to breakage	Short C-shaped chips, prone to breakage	Smaller C-type chips
Experiment	Long strip-shaped chips that are not easily broken	Long C-shaped chips	Collapsed debris
Determine value	**Spindle speed 480r/min, chip depth 0.3mm**		
Feed speed	0.5m/min	0.8m/min	1.0m/min
Simulation	Short C-shaped chips, prone to breakage	Long C-shaped chips	Strip shaped chips, curled, not easily broken
Experiment	Short C-type chips+a small amount of debris	Long C-shaped chips	Strip shaped chips, narrow and sharp

Table 1 displays that the influence of SS and feed speed (FS) on the chip is significantly greater than the DOC. When the DOC is 0.3mm and the FS is 1.0m/min, the larger the SS is, the smaller the chip is, and the easier it is to break and crumble. Furthermore, FS has the opposite effect on the chip state. The larger the FS, the more robust the chip is.

Moreover, the angle of the tool itself affects the frictional resistance and heat of the workpiece, so the front and back angle of the tool is varied in order to analyze the CF. Fig. 7 displays the findings.

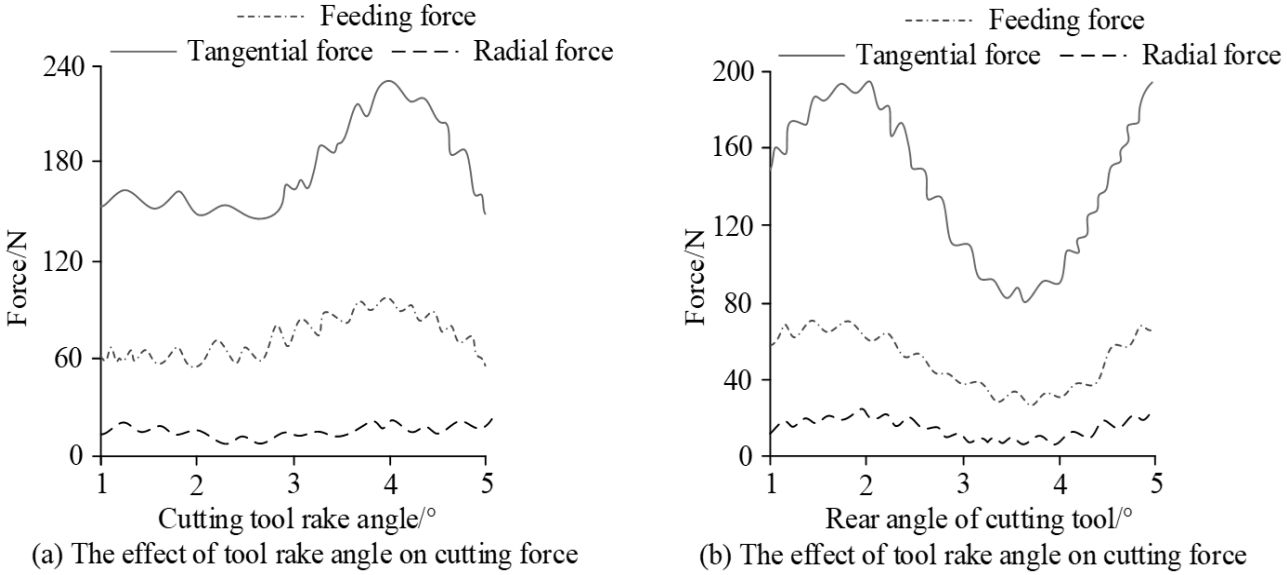

Fig. 7 *The effect of CF on the front and rear angles of the tool*

Fig. 7(a) shows that when the tool front angle is at 4°, both the feed force and tangential force reach the maximum moment value, which are 97.5N and 225N, respectively. Moreover, the change of tangential force is most obvious. Fig. 7(b) shows a small peak of CF when the front angle is kept at 2° and the back angle at 2°, where the result of radial force is 22N. In conclusion, the variation of CF is related to the frictional resistance between the tool and the workpiece. To reduce the accumulation of chips, the front angle should be selected from 1° to 3° and the rear angle from 3° to 4°.

3.2 Simulation tests of residual stress and machining quality analysis

To improve the surface quality of the finished turned part TA, it is necessary to analyze the surface roughness (SR) RS of the part since it has a direct effect on the strength and wear resistance of the part material. To measure and record the RS on the surface of the TA workpiece, an X-ray stress analyzer is used in this study. The test is shown in Fig. 8.

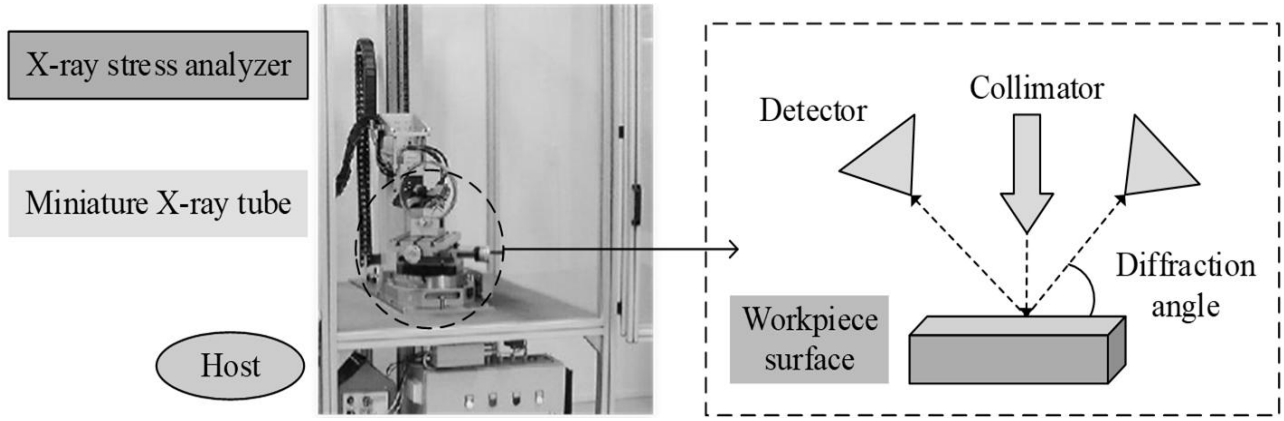

Fig. 8 *Configuration of residual stress measurement using X-ray diffraction method*

Fig. 8 shows the selection of Xstress 3000 model X-ray stress analyzer for the test analysis. It mainly consists of main unit, micro X-ray tube, goniometer, and detector. When X-rays are irradiated on the surface of the workpiece, the detector will pick up the peaks of the reflected light from the X-rays at a specific angle. When the cutting operation of the TA workpiece is completed, the two ends of the workpiece are more likely to be affected by the stress of the machining process due to the uneven distribution of RS inside the workpiece. Therefore, the two ends are chosen to better reflect the RS state during the measurement.

After measuring the RS of a real TA material, the study first ensures that the simulation parameters are consistent with the measured ones to minimize errors. Multiple, independent measurements are then taken of the workpiece material measurement points, and their average values are recorded and calculated. This reflects the overall level of RS, which reduces random errors and improves the reliability of both simulation and measurement data. Table 2 displays the findings.

Tab. 2 *Simulation results of residual stress under different factors*

Spindle speed (r/min)	Residual stress/Mpa	Feeding speed (m/min)	Residual stress/Mpa	Cutting depth (mm)	Residual stress/Mpa
520 r/min	-145Mpa	0.5 m/min	-387Mpa	0.10 mm	20Mpa
560 r/min	-147Mpa	0.6 m/min	-380Mpa	0.15 mm	15Mpa
600 r/min	-140Mpa	0.7 m/min	-377Mpa	0.20 mm	10Mpa
640 r/min	-138Mpa	0.8 m/min	-374Mpa	0.25 mm	-65Mpa
680 r/min	-210Mpa	0.9 m/min	-255Mpa	0.30 mm	-140Mpa
720 r/min	-235Mpa	1.0 m/min	-140Mpa	0.35 mm	-135Mpa
760 r/min	-310Mpa	1.1 m/min	-155Mpa	0.40 mm	-125Mpa
800 r/min	-345Mpa	1.2 m/min	-150Mpa	0.45 mm	-115Mpa

Table 2 shows that when the SS increases from 640 r/min to 680 r/min and 720 r/min, the workpiece surface rubs violently against the tool. The contact surface generates great heat and vibration, which in turn causes rapid increase in RS. When the tool travel speed is from 0.8m/min to 1.0m/min, the cutting heat increases and the stress of the workpiece material changes dramatically. Moreover, the DOC is between 0.2mm to 0.3mm, and the friction between the tool and the workpiece material generates a large amount of cutting heat and RS.

The best cutting settings to enhance the machining quality of TA workpieces are then determined by comparing the simulation and experimental outcomes. The results are shown in Fig. 9.

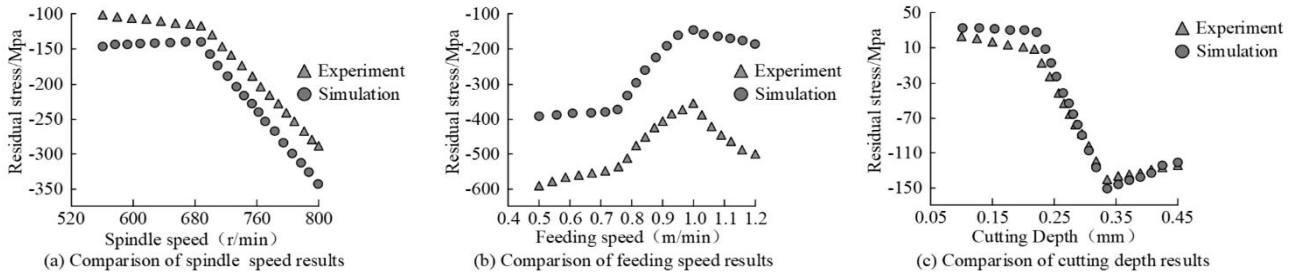

Fig. 9 *Comparison of residual stress results under different factors*

Fig. 9(a) shows that the maximum value of RS is reached when the speed of traveler is 640 r/min with simulation and test results of -138Mpa and -105Mpa, respectively. Fig. 9(b) shows that when the tool travel speed is 1.0 m/min, the workpiece is subjected to maximum RS with simulation and test results of 140Mpa and -350Mpa, respectively. Fig. 9(c) shows that when the DOC is 0.2 mm, the RS results are maximum in simulation and test results and are 10Mpa and 30Mpa, respectively. In conclusion, the optimum of RS on process parameters lies between 520 r/min to 680 r/min SS, 1.0 m/min travel speed and 0.2 mm DOC.

Finally, the SR formed by the TA turning process is tested to compare the simulated and actual roughness when the SS is 480 r/min. The results are shown in Fig. 10.

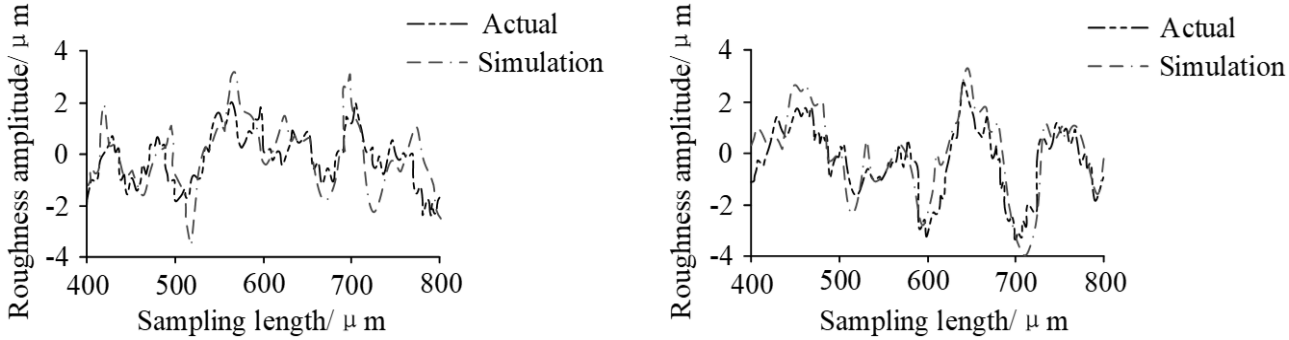

Fig. 10 *Comparison of surface roughness between simulation and actual results*

Fig. 10(a) shows that the SR simulation results of TA workpiece at fixed SS and DOC with travel speed of 1.0 m/min are between -4 μm and 4 μm. Moreover, the highest roughness is obtained when the sampling length is 600μm or 700μm, which is 3μm and 3.1μm, respectively. In Fig. 10(b), it is shown that the SR of the TA workpiece roughness basically agrees with the trend of the actual measurement when the DOC is 0.2mm. When the sampling length is 650 μm, the roughness results of actual and simulation are 3 μm and 3.1 μm, respectively, and the difference between them is small. In summary, the SR results of the simulation test are basically consistent with the actual measurement outcomes, which can provide the best process parameters for the improvement of machining quality.

4 Discussion

In the field of machining, TAs have become the prime equipment material for industrial and other cutting-edge industries, and are widely used in the fabrication of components in advanced fields due to their low density, high strength, and high corrosion resistance. The study utilized FEA to deal with the TA turning process, using the intrinsic equations and material calculations in ABAQUS software to build a three-dimensional simulation model. Afterwards, the process parameters of the turning process were explored to analyze the surface quality and machinability of the TA workpiece. In the comparative analysis of RS and machining quality, the best choice of process parameters for the simulation analysis of RS was in SS, tool travel speed, and DOC. This was due to the fact that during the cutting process, the tool-material interaction, vibration of the cutter tool in the tool tray, and the shape of the chips affect the quality of the surface of the workpiece. This in turn caused some damage to the machining accuracy, wear strength and service life of the workpiece. In the study of Zou Z et al. on chip morphology of TA turning, an intrinsic model of hyperbolic tangent function was utilized to define the material properties, which yielded an average CF improvement of 3.8% and a chip serration error of 17.4% [20]. Whereas, the study analyzed the chip morphology in terms of SS, tool travel speed, and DOC. The results yielded an average error of 12.03%

for CF, which was lower than the above results. Therefore, the FEA and the intrinsic equations proposed by the study were superior for the titanium turning process on centerless lathe, which was important for the quality enhancement and performance improvement in the field of industrial mechanical parts machining.

5 Conclusion

In response to the machining process and quality issues of TA materials, a study proposed the use of FEA and ABAQUS software to develop a centerless lathe precision turning model for TA workpiece machining, filling the research gap in this area. Moreover, using constitutive equations and material property calculations, experiments were conducted on the CF and RS of centerless lathe process parameters. During the turning process, simulation analysis was conducted on CF and chip morphology. The results showed that the average error of SS on CF was 16.66%, while the average errors of cutting speed and cutting depth on CF were 8.21% and 11.22%, respectively, which were relatively small. The maximum difference between the SR simulation and the actual measurement was only 0.1 μm, which further indicated that the proposed model has high accuracy. After optimization, the SS was 520-680 rpm, the cutting speed was 1.0 m/min, and the cutting depth was 0.2 mm, proving that the proposed model could significantly improve the machining quality. The proposed centerless precision turning model had superior performance. However, this study mainly focused on CF, RS and surface quality, and lacked the analysis of cutting heat control and actual machining environment factors. Meanwhile, the accuracy of the model may decrease under extreme process parameter conditions, and future research needs to further expand the application scope of the model. Future research will further improve the model to comprehensively consider the effects of cutting heat and environmental factors, and further improve the accuracy and applicability of the model.

Acknowledgement

The research is supported by School Grants platform for Scientific Research of Shandong Huayu University of Technology in 2019: CNC tool manufacturing process research and development center.

References

[1] WU, Y., HE, W., MA, H., NIE, X., LIANG, X., PAN, J., WANG, S., SHANG, M., CHENG, L. (2024). Titanium Alloy Materials with Very High Cycle Fatigue: A Review. In: *Materials*, Vol. 17, No. 12, pp. 1–37.

[2] TEBALDO, V., GIOVANNA, G. D. C., DURACCIO, D., FAGA, M. G. (2024). Sustainable Recovery of Titanium Alloy: From Waste to Feedstock for Additive Manufacturing. In: *Sustainability*, Vol. 16, No. 1, pp. 1–28.

[3] AGEEV, E. V., AGEEVA, E. V., AGEEVA, A. E., SEREBROVSKI, V. I. (2023). Physical and Mechanical Properties of a Tungsten-Titanium-Cobalt Alloy Produced by Spark Plasma Sintering of Hard-Alloy Electroerosive Powders Produced in Kerosene. In: *Metallurgist*, Vol. 67, No. 3/4, pp. 526–531.

[4] LI, Z., WANG, Q., DU, X., YANG, C., WANG, K. (2024). Thermal Deformation Behavior and Microstructural Evolution Mechanism of TC4 Titanium Alloy Based on Hot Processing Map. In: *JOM*, Vol. 76, No. 9, pp. 5233–5246.

[5] YANG, Y., WANG, Y., SUN, C., WU, Q., YAN, J., LIU, Y., YAO, J., ZHANG, W. (2024). Processing of Titanium Alloys with Improved Efficiency and Accuracy by Laser and Electrochemical Machining. In: *The International Journal of Advanced Manufacturing Technology*, Vol. 130, No. 7, pp. 4013–4025.

[6] XIAO, G., ZHU, S., HE, Y., LIU, G., NI, Y. (2023). Thermal-Mechanical Effect and Removal Mechanism of Ti-6Al-4V During Laser-Assisted Grinding. In: *Chinese Journal of Mechanical Engineering*, Vol. 36, No. 5, pp. 77–96.

[7] AHMAD, A., AKRAM, S., JAFFERY, S. H. I., KHAN, M. A. (2023). Evaluation of Specific Cutting Energy, Tool Wear, and Surface Roughness in Dry Turning of Titanium Grade 3 Alloy. In: *The International Journal of Advanced Manufacturing Technology*, Vol. 137, No. 3, pp. 1263–1274.

[8] YANG, H., WANG, Z. (2023). The Different Electroplastic Effects of Cutting Directions During the Turning Process of Ti-6Al-4V Titanium Alloy. In: *International Journal of Materials & Product Technology*, Vol. 67, No. 2, pp. 155–165.

[9] WANG, D., CHEN, X., LAI, X., ZHAO, G., YANG, Y. (2023). Effect of Cutting Surface Integrity on Fatigue Properties of TC17 Titanium Alloy. In: *Materials*, Vol. 16, No. 16, pp. 1–14.

[10] PALANIVEL, R., DINAHARAN, I., LAUBSCHER, R. F., ALSWAT, H. M. (2024). Influence of Micro-Textured Polycrystalline Diamond Tools on the Machining Performance of Titanium Alloy Ti-6Al-4V in Dry

Turning. In: *International Journal of Advanced Manufacturing Technology*, Vol. 132, No. 9/10, pp. 4297–4313.

[11] LI, L., SUN, S., XING, W., ZHANG, Y., WU, Y., XU, Y., WANG, H., ZHANG, G., LUO, G. (2024). Progress in Simulation Modeling Based on the Finite Element Method for Electrical Discharge Machining. In: *Metals*, Vol. 14, No. 1, pp. 1–34.

[12] YU, H., HE, Z., LI, J., LI, B., XIN, J., YAO, L., YAN, F. (2023). Finite Element Modeling on Micro-Machining of Graphene-Reinforced Aluminum Matrix Composites. In: *The International Journal of Advanced Manufacturing Technology*, Vol. 124, No. 1, pp. 97 – 110.

[13] GROSSI, N., SCIPPA, A., CAMPATELLI, G. (2024). Diametral Error Correction in Turning Slender Workpieces: An Integrated Approach. In: *International Journal of Advanced Manufacturing Technology*, Vol. 130, No. 4, pp. 1393–1404.

[14] SURANI, K., PATEL, S., MOUNAGURUSAMY, M. K., ZAHRA, M. M. A., PANCHAL, H., SIDDIQUI, M. I. H., SHAH, M. A., NATRAYAN, L., KUMAR, A. (2024). Numerical Analysis of the Powder Mixed Electrical Discharge Machining (PMEDM) Process for TZM-Molybdenum Superalloy Using Finite Element Method. In: *AIP Advances*, Vol. 14, No. 2, pp. 1–15.

[15] OLLER, S., NALLIM, L. G., BELLOMO, F. J., RUANO, G. (2023). A Theoretical Homogenized Constitutive Model Formulation for Matrix Composite Materials Reinforced with Curved Fibers. In: *Composite Structures*, Vol. 304, No. 2, pp. 116432–116441.

[16] GAN, S. M., HAN, Y. Q., BAO, X. Y. (2022). Influence of Energy Ratio of Hybrid Heat Source on Residual Stress Distribution of 7A52 Aluminum Alloy VPPA-MIG Hybrid Welding. *Manufacturing Technology*, Vol. 22, No. 3, pp. 279-287.

[17] ERUM, N., AHMAD, J. (2024). Structural, Elastic and Mechanical Properties of Cubic Perovskite Materials. In: *Archives of Advanced Engineering Science*, Vol. 2, No. 1, pp. 24–29.

[18] ZHAO, X., LI, C., TANG, Y., LI, X., CHEN, X. (2024). Reinforcement Learning-Based Cutting Parameter Dynamic Decision Method Considering Tool Wear for a Turning Machining Process. In: *International Journal of Precision Engineering and Manufacturing-Green Technology*, Vol. 11, No. 4, pp. 1053–1070.

[19] KAROLCZAK, P. (2023). Analysis of Cutting Forces with Application of the Discrete Wavelet Transform in Titanium Ti6Al4V Turning. *Manufacturing Technology*, Vol. 23, No. 4, pp. 449-460.

[20] ZOU, Z., HE, L., ZHOU, T. T. P. Z. T. (2024). Research on Serrated Chip Morphology for Turning Ti6Al4V Titanium Alloy by Considering Damage Evolution. In: *Journal of Manufacturing Processes*, Vol. 118, No. 5, pp. 283–301.